

Supplementary

An over 10% module efficiency using non-Bi₂Te₃ thermoelectric materials for recovering heat of <600 K

Zhonglin Bu, Xinyue Zhang, Yixin Hu, Zhiwei Chen, Siqi Li, Wen Li and Yanzhong Pei*

Interdisciplinary Materials Research Center, School of Materials Science and Engineering, Tongji Univ., 4800 Caoan Rd.,
Shanghai 201804, China.

*Email: yanzhong@tongji.edu.cn

Materials and Methods

Synthesis:

Polycrystalline p-type (Ge_{0.98}Cu_{0.04}Te)_{0.88}(PbSe)_{0.12} and n-type Mg_{3.05}Y_{0.015}SbBi are synthesized by melting and annealing. High-purity elements Ge (99.99%), Cu (99.999%), Te (99.99%), Pb (99.999%) and Se (99.99%) were weighted according to the composition of (Ge_{0.98}Cu_{0.04}Te)_{0.88}(PbSe)_{0.12}. The raw materials were loaded into a quartz tube that was sealed and placed in a furnace at 1223 K for 5 hours, followed by quenching in cold water and annealing at 843 K for 72 hours and then quenching in water. Similarly, high-purity elements Mg (99.99%), Y (99.99%), Sb (99.99%), Bi (99.99%) were weighted according to the composition of Mg_{3.05}Y_{0.015}SbBi, the raw materials were sealed in a tantalum tube and then sealed in a quartz ampoule. The ampoule was then placed in a furnace at 1323 K for 5 hours, followed by quenching in cold water and annealing at 923 K for 72 hours and then quenching in water. The obtained (Ge_{0.98}Cu_{0.04}Te)_{0.88}(PbSe)_{0.12} and Mg_{3.05}Y_{0.015}SbBi ingots were ground into fine particles for hot pressing. The (Ge_{0.98}Cu_{0.04}Te)_{0.88}(PbSe)_{0.12}, SnTe and Ag powders were loaded to a graphite die for one-step hot-pressing at 723 K for 60 minutes under a uniaxial pressure of ~50 MPa. A similar approach is applied for Mg_{3.05}Y_{0.015}SbBi with Fe electrode and Ni diffusion barrier layer, and the one-step hot pressing was done at 823 K for 90 minutes under a uniaxial pressure of ~90 MPa. The obtained Ag/SnTe/(Ge_{0.98}Cu_{0.04}Te)_{0.88}(PbSe)_{0.12}/SnTe/Ag and Ni/Fe/Mg_{3.05}Y_{0.015}SbBi/Fe/Ni cylinders with a dimension of ~12 mm in diameter and ~6 mm in thickness (Ag or Ni layer: ~0.9 mm, SnTe or Fe layer: ~0.1 mm). The synthesis of SnTe can be found in the literature¹. The Ag, Fe and Ni powders used as diffusion layers or electrodes came directly from a commercial source with a particle size of 200 mesh.

The obtained n- and p-type cylinders were then sliced into plates and bars using a Wire-Cutting-Machine for characterizations, transport-property measurements and module fabrication. The processing could lead to a change in properties. In addition to the temperature and pressure of hot pressing, the crystallinity, density and duration of pressing could all play an important role. In this work, the density of the materials (without electrode and diffusion-barrier) is higher than 97%, enabling the high thermoelectric performance (**Fig. 1**).

Characterizations and transport-property measurements:

The phase composition and microstructure of the materials were characterized by X-Ray diffraction (XRD, DX2000) and Scanning Electronic Microscopy (SEM, Phenom Pro) equipped with an Energy Dispersive Spectrometer (EDS). The microstructure of the Ag/SnTe/GeTe and Ni/Sb/Mg₃SbBi junctions were characterized by SEM and EDS. Simultaneous temperature dependent resistivity and Seebeck coefficient were measured under helium, the resistivity was measured by a four-probe Van Der Pauw technique, and the Seebeck coefficient was obtained from the slope of thermopower versus temperature gradient. The thermal conductivity (κ) is determined by $\kappa = dCpD$, where d , Cp , D are the density (estimated by mass/volume), heat capacity and thermal diffusivity (measured by a laser flash technique, Netzsch LFA467). Both electronic and thermal transport properties were performed in the temperature range of 300-650 K. The uncertainty for the measurements of S , ρ , κ is about 5%.

Contact resistance measurements:

The contact resistance (R_c) of the p- and n-type legs were measured using a home-made four-probe measurement system². The leg with diffusion layers and electrodes was scanned from the thermoelectric materials towards the electrodes while the voltage was recorded at a constant electrical current of 100 mA. The contact resistance (R_c) is estimated by the sudden change in voltage from thermoelectric materials to electrodes.

Module fabrication and efficiency measurements:

The p- and n-type legs with a cross-section area of ~1.5×1.5 mm² were sliced from the cylinders (**Fig. S1**). The p- and n-type legs were alternately positioned onto an insulated alumina ceramics (Al₂O₃) with a dimension of 10 mm × 10 mm × 0.65 mm, and Cu plates was used as the connecting bridge for p- and n-type legs. The welding at the hot side is done by a Sn-Sb-Pb solder (melting point of ~360 °C) while the cold side by a tin-based solder (melting point of ~210 °C). Two Cu wires were soldered to the cold-side Cu plates to supply current and measure the terminal voltage.

The output power (P) and conversion efficiency (η) of the (Ge_{0.98}Cu_{0.04}Te)_{0.88}(PbSe)_{0.12}/Mg_{3.05}Y_{0.015}SbBi module under different temperature gradients were measured in vacuum by a home-made measurement system (**Fig. S2**)². The cold-side temperature was maintained at 280 K by a cooling system. A graphite paper (0.2 mm thick) and thermal grease (QM850) were used at the hot-side between the heater and the module, and at the cold side between the module and heat-flow meter, to improve the thermal conduction. Two K-type thermocouples (Omega) were respectively adhered between the heater and the module and between the module and heat-flow meter, for measuring the hot (T_h) and cold (T_c) side temperatures crossing the module.

The heating system used two tubular heaters (Omega) embedded in a graphite block at the hot side. The cooling block used circulating water along with a thermoelectric cooling plate at the cold side. An oxygen-free Cu block with known thermal conductivity (κ_{Cu})² having a cross-section area of 10 mm×10 mm was used as a heat flow meter for measuring the heat flow (Q) through the thermoelectric module. Two tiny K-type thermocouple probes (Omega) with a diameter of only 0.6 mm for reducing

the heat loss were embedded in the heat flow meter with a further soldering, at a vertical distance of 17 mm to measure the temperature drop along the heat flow direction. In order to ensure the accuracy in determining the temperature difference of the heat-flow meter, each thermocouple takes 60 measurements for averaging (**Fig. S3a**), the linear relationship between ΔT and ΔT_{Cu} (**Fig. S3b**) nicely suggests the consistent responsibility of the heat-flow meter. As shown in **Table S1**, the relative standard deviation (RSD) for these 60 measurements can be ensured to be within 3.5%. The heat flow (Q) was estimated in accordance with one-dimensional Fourier's law:

$$Q = \frac{\kappa_{Cu} A_{Cu}}{L_{Cu}} \Delta T_{Cu} \quad , \quad S1$$

where Q , A_{Cu} , L_{Cu} , $\Delta T_{Cu}=T_1-T_2$ and κ_{Cu} are the heat flow, cross-sectional area of the heat-flow meter, distance between the thermocouples, temperature difference and thermal conductivity of the heat-flow meter (Cu block).

A measurement of thermoelectric efficiency was enabled by measuring the output power ($P=IV$) and the heat flow in vacuum, where I is the current and V is the output voltage. By varying the external load resistance and measuring the corresponding load voltage and current, the maximum output power can be obtained. Therefore, the efficiency (η) can be estimated according to $\eta=P/(P+Q)$. To minimize the system error, we measured each parameter (including temperature, voltage and current) for 60 times for averaging. The heater, module and heat-flow meter were assembled under a uniaxial pressure to improve the thermal conduction and that a high vacuum below 10^{-6} mbar is needed for reducing heat convection.

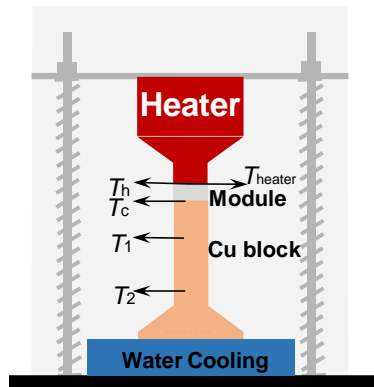


Fig. S1. Schematic for the setup measuring the output power and efficiency of the thermoelectric module.

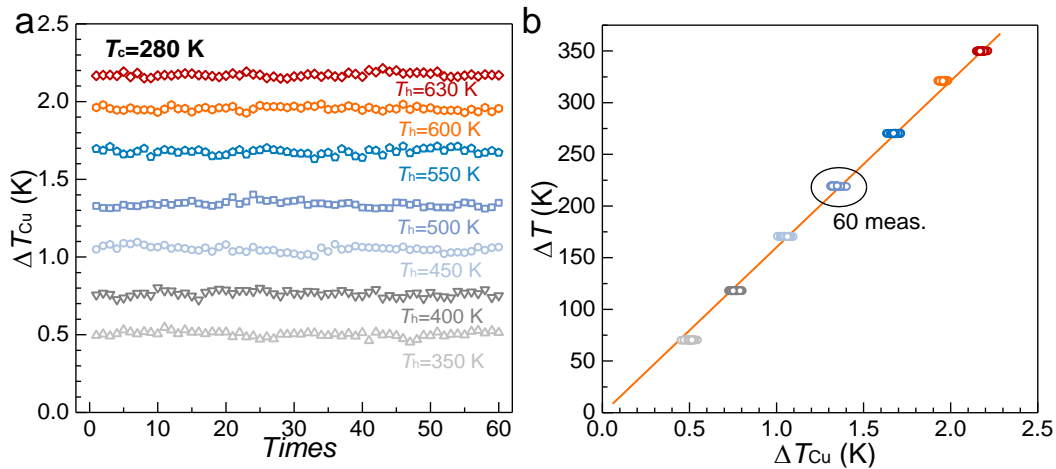


Fig. S2. Temperature differences of the heat-flow-meter (ΔT_{Cu}) under different temperature differences (ΔT) applied to the thermoelectric module (a) and the relationship between (b).

Table S1. The temperature difference applied to the module (ΔT) and the corresponding temperature difference for the heat-flow meter (ΔT_{Cu}) of 60 measurements for averaging and its Relative Standard Deviation (RSD) of the heat-flow meter. The estimated uncertainty of ΔT_{Cu} , measured heat flow (Q), and conversion efficiency (η) of the module in this work.

ΔT (K)	ΔT_{Cu} (K)	RSD (%)	Uncertainty of ΔT_{Cu} (%)	Uncertainty of Q (%)	Uncertainty of η (%)
70	0.5	3.36	9.94	16.1	17.6
120	0.76	3.18	6.53	13	13.1
170	1.05	1.86	4.75	11.3	10.82
220	1.34	1.33	3.74	10.36	9.51
270	1.68	1.13	2.98	9.65	8.56
320	1.95	0.86	2.56	9.26	7.95
350	2.17	0.65	2.3	9.02	7.64

Estimation of heat radiation and leakage:

The heat radiated from the surfaces of legs to the surroundings (horizontal) can be estimated by the following equation^{3,4}:

$$Q_{rad} = \frac{\varepsilon\theta C}{\Delta T} \int_{T_c}^{T_h} (T^4 - T_s^4) dT \quad S2$$

where the Q_{rad} is the heat radiation, ε is the emissivity, θ is the Stefan-Boltzmann constant, C is the total surface area, ΔT is the temperature gradient, T_h is the hot-side temperature, T_c is the cold-side temperature, T is the temperature distribution, and T_s is the surrounding temperature. The emissivity of 0.5 is used according to the previous reports of thermoelectric materials³⁻⁵. The surrounding temperature ranges from 300-320K, therefore an average of 310 K is used for simplicity. The estimated heat radiation increases with increasing temperature, leading to a significant loss of 10.5% at $T_h=600$ K and $T_c=280$ K (unmeasurable by the heat-flow meter). Similarly, heat radiation from the unfilled hot-side substrate to the cold-side one (vertical), which is measurable by the heat-flow meter, can be estimated to be 12.4% at the same temperature gradient.

Note that the heat-flow meter locates underneath the cold side of the module having a temperature lower than the surrounding temperature, heat transferred from the surroundings to the heat-flow meter is estimate to be only about 0.9% of Q . Heat leakages due to thermal conduction of wires attached to the module and heat-flow meter can be estimated from Fourier's law, which are not greater than 1.6% of Q in this work.

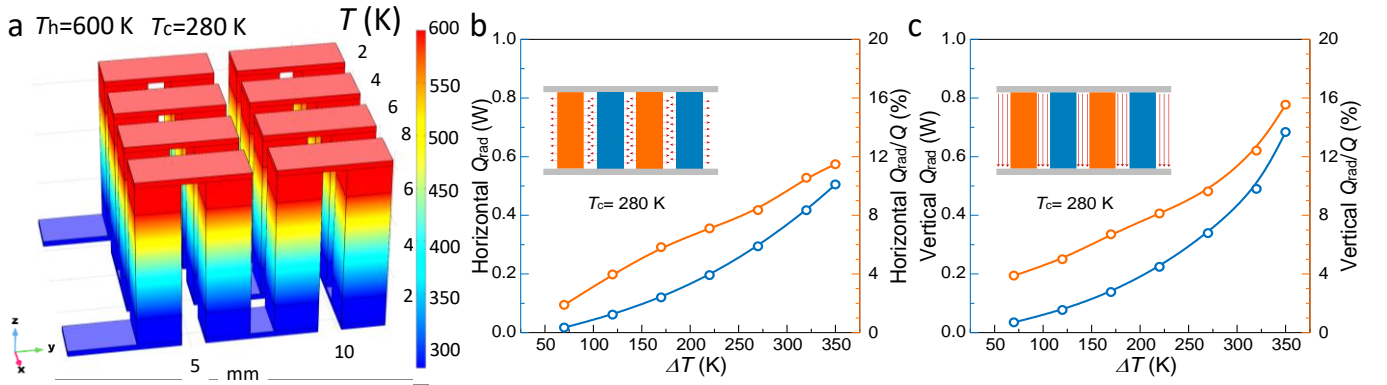


Fig. S3. Temperature distribution in the module (a), temperature gradient dependent horizontal (b) and vertical (c) radiation heat.

Uncertainty analyses:

The measurement of κ_{Cu} by LFA 457 involves an uncertainty of 5%² and the uncertainties of A_{Cu} and L_{Cu} are 1% and 0.5%, respectively. To ensure the sufficiently high sensitivity of ΔT_{Cu} of the heat-flow meter, intentionally varied T_h and T_c of the module with a constant temperature gradient indeed leads to variations in T_1 and T_2 of the heat meter but ΔT_{Cu} does not show unacceptable fluctuations. This is illustrated by the relationship between T_1 and T_2 , which confirms stabilized $\Delta T_{Cu}=T_2-T_1$ at a given temperature gradient applied to the module (**Fig. S5**). Note that the uncertainty of ΔT_{Cu} decreases with increasing temperature gradient (ΔT), leading to a small uncertainty of 2.56% at $\Delta T=320$ K (**Table S1**). As a result, the uncertainty of Q is about 9% at this temperature gradient. Output power of the module is determined by the current (I) and output voltage (V) with an uncertainty of less than 1%. The open-circuit voltage (V_{oc}) responds quickly to the hot-side temperature (**Fig. S6**), further ensures the high responsibility of the measurement setup. The overall uncertainty of efficiency measurement ranges from 18% to 8% in this work, depending on the temperature gradients applied to the module, and a larger temperature gradient helps reduces the uncertainty (**Table S1**).

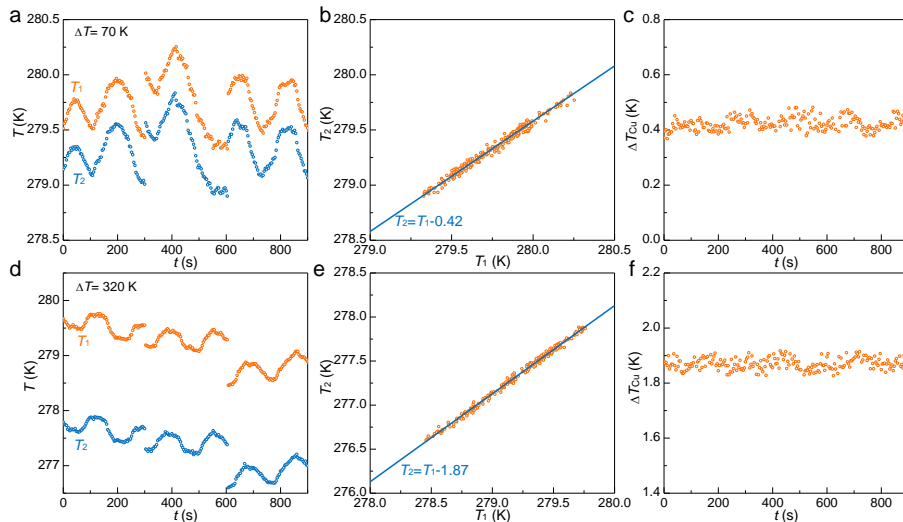


Fig. S4. Temperature responsibility of the heat-flow meter under intentionally varied T_h and T_c with constant temperature gradients of 70 (a, b and c) and 320 K (d, e and f).

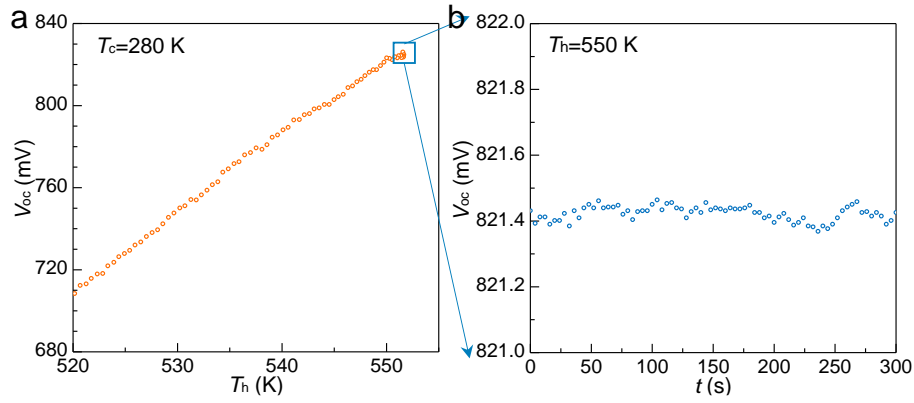


Fig. S5. Hot-side temperature (T_h) (a), and time (t) dependent open-circuit voltage (V_{oc}).

Calibration of the module measurement system:

In this work, the measurement accuracy has also been checked with the results measured by the commercial instruments. In more details, two commercial Bi_2Te_3 modules TEG31 from SAGREON Technology⁶ are used as the standard ones for checking the measurement accuracy. The dimensions of the commercial Bi_2Te_3 modules are $12 \times 12 \times 3.8$ mm³. The modules' properties include output voltage, current and heat-flow are measured at different temperature gradients by different apparatus (**Fig. S6, S7**). The output power $P=VI$ of two modules measured by our setup and by Mini-PEM (Advance Riko, Japan) are quite comparable, indicating the nice accuracy here in electrical properties measurements. More importantly, the heat-flow (Q) measured by our system is also nicely consistent with that by Mini-PEM. This leads the maximum conversion efficiencies (η_{\max}) of the commercial Bi_2Te_3 module measured by different apparatus and that disclosed by SAGREON to be almost the same, ensuring the accuracy of the technique here for measuring the efficiency (**Fig. S8**).

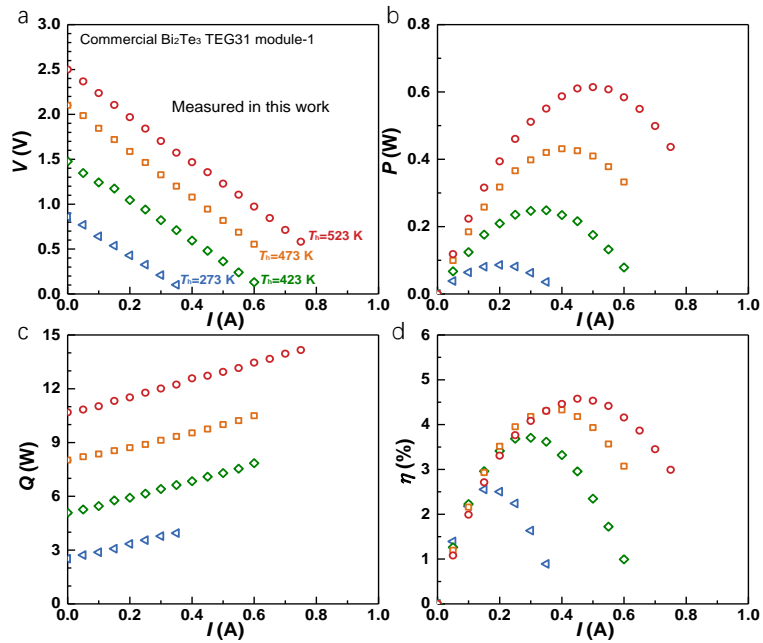


Fig. S6. Current I dependent output voltage V (a), power P (b), heat flow Q (c), and conversion efficiency η (d) under different temperature differences for commercial Bi_2Te_3 module TEG31 measured in this work.

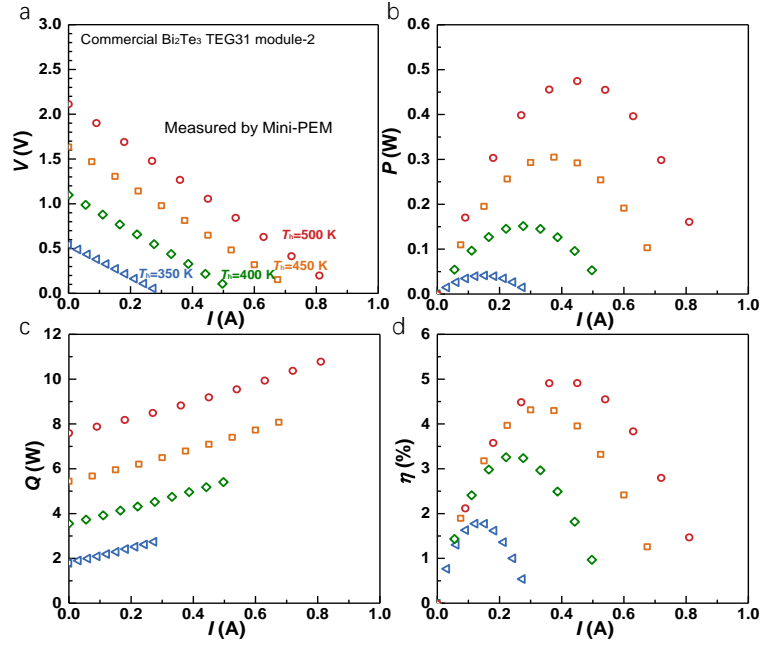


Fig. S7. Current I dependent output voltage V (a), power P (b), heat flow Q (c), and conversion efficiency η (d) under different temperature differences for commercial Bi_2Te_3 module TEG31 measured by Mini-PEM.

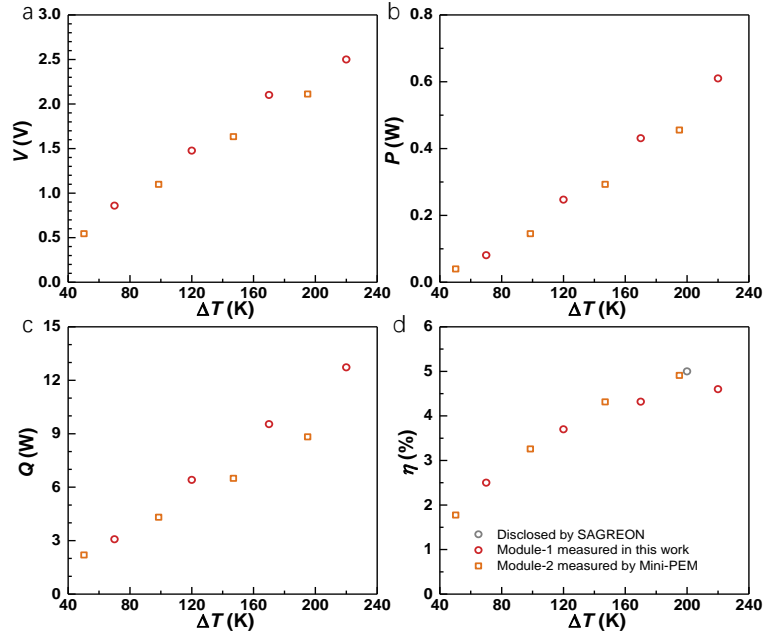


Fig. S8. Temperature gradient dependent open-circuit voltage V (a), power P (b), heat flow Q (c), and maximum efficiency η_{\max} (d) for commercial Bi_2Te_3 TEG31 modules measured in this work and by Mini-PEM, with a comparison to that disclosed by SAGREON⁶.

Prediction of conversion efficiency:

The module performance in this work is estimated by a simplified analytical one-dimensional model^{3,7}. The internal resistance of module (R_{in}) and the resistance of the thermoelectric materials ($R_{\text{materials}}$) are:

$$R_{in} = R_{\text{material}} + R_{\text{contact}} \quad \text{S3}$$

$$R_{\text{material}} = N \left(\frac{H}{A_p \bar{\rho}_p} + \frac{H}{A_n \bar{\rho}_n} \right) \quad \text{S4}$$

where the R_{contact} is contact resistance, N is pairs of couples, H is height of the thermoelectric legs, A_p is cross-sectional area of p-leg, A_n is cross-sectional area of n-leg, $\bar{\rho}_p$ is the average resistivity of p-type material and $\bar{\rho}_n$ is the average resistivity of n-type material.

The open-circuit voltage (V_{oc}) of the module is:

$$V_{oc} = N(T_h - T_c)(\bar{S}_p - \bar{S}_n) \quad \text{S5}$$

where the T_h is hot-side temperature, T_c is cold-side temperature, \bar{S}_p is average Seebeck coefficient of p-type material, and \bar{S}_n is

average Seebeck coefficient of n-type material.

The output power (P) of the module is:

$$P = (V_{oc} - R_{in}I)I \quad S6$$

where the I is the current.

The open-circuit heat-flow (Q_{oc}) of the module is:

$$Q_{oc} = N\left(\frac{A_p}{H}\bar{\kappa}_p + \frac{A_n}{H}\bar{\kappa}_n\right) \quad S7$$

where $\bar{\kappa}_p$ is the average thermal conductivity of p-type material, and $\bar{\kappa}_n$ is average thermal conductivity of n-type material.

The input heat at the hot-side (Q_{input}) of the module:

$$Q_{input} = Q_{oc} - \frac{R_{in}I^2 + N(\beta_p + \beta_n)T_hI}{2} + N[S_p(T_h) - S_n(T_h)]T_hI \quad S8$$

$$\beta_n = \frac{T_c}{T_h} [S_n(T_c) - \bar{S}_n] + [\bar{S}_n - S_n(T_h)] \quad S9$$

$$\beta_p = \frac{T_c}{T_h} [\bar{S}_p - S_p(T_c)] + [S_p(T_h) - \bar{S}_p] \quad S10$$

where β_p and β_n are combined coefficient of p-type and n-type materials, respectively.

The conversion efficiency (η) of the module can be estimated by:

$$\eta = \frac{P}{Q_{input}} = \frac{P}{Q + P} \quad S11$$

where Q is heat-flow from cold-side of the module. The prediction of η and Q are shown in **Fig. 4** and **Fig. S15**.

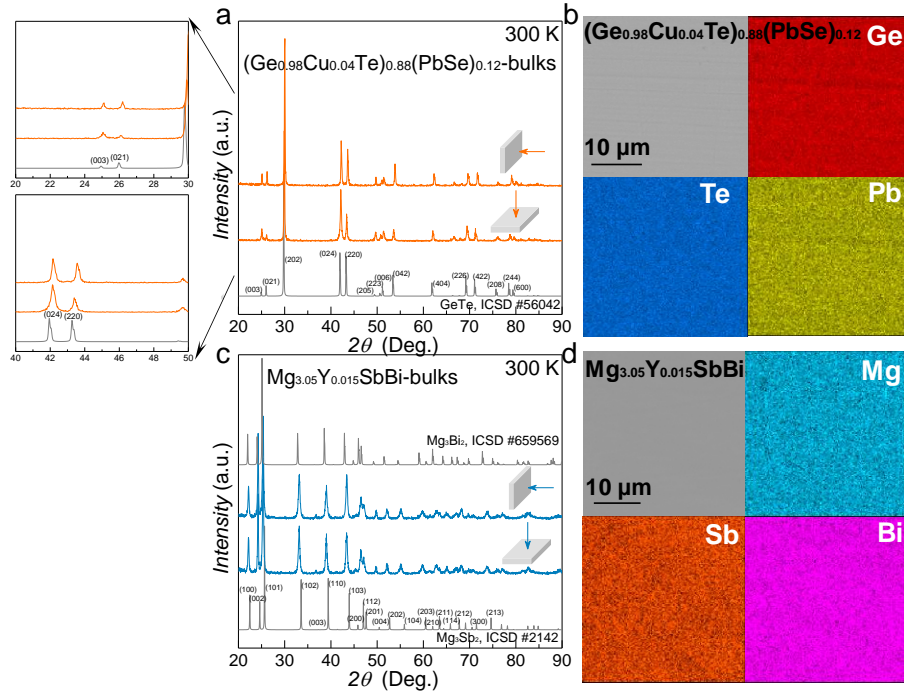


Fig. S9. Room temperature XRD patterns (a, c), back-scattering scanning electron microscope (SEM) images and the corresponding energy dispersive spectroscopy (EDS) compositional mapping (b, d) for p-type $(\text{Ge}_{0.98}\text{Cu}_{0.04}\text{Te})_{0.88}(\text{PbSe})_{0.12}$ (a, b) and n-type $\text{Mg}_{3.05}\text{Y}_{0.015}\text{SbBi}$ (c, d).

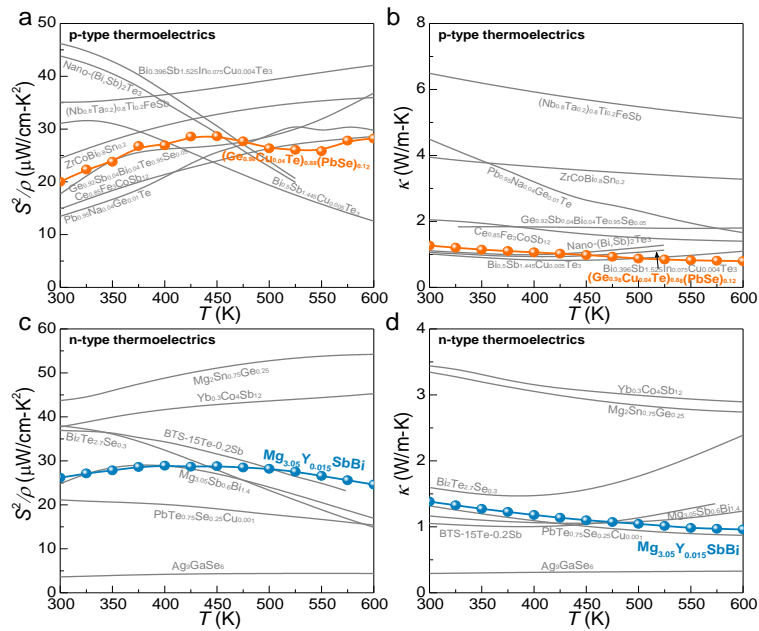


Fig. S10. Temperature dependent power factor (S^2/ρ) (a, c) and thermal conductivity (κ) (b, d) for p-type thermoelectrics⁸⁻¹⁵ (a, b) and n-type ones^{10, 12, 16-20} (c, d).

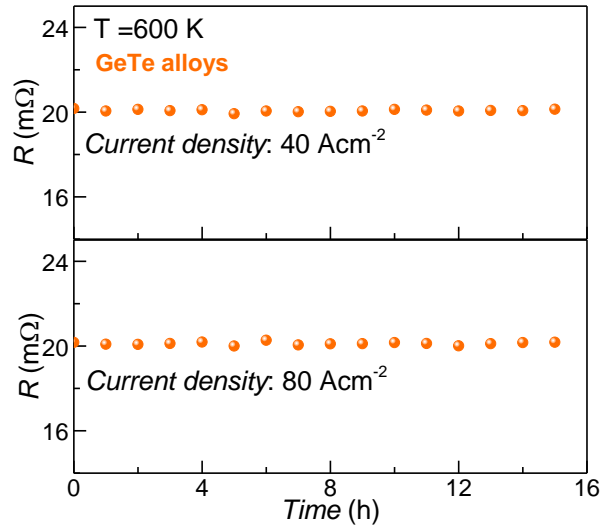


Fig. S11. Resistance of $(\text{Ge}_{0.98}\text{Cu}_{0.04}\text{Te})_{0.88}(\text{PbSe})_{0.12}$ under large current densities 40 and 80 A cm^{-2} at 600 K for up to 16 hours.

Table S2. The parameters used for the simulation.

Parameters	$T_h=400\text{ K}$	$T_h=500\text{ K}$	$T_h=600\text{ K}$
Total cross-sectional area A_{np} (mm^2)	4.5	4.5	4.5
P-leg electrical contact resistivity (mW cm^2)	10	10	10
N-leg electrical contact resistivity (mW cm^2)	15	15	15
Thermal contact resistance of cold-side ($\text{W/m}^2\text{K}$)	10^4	10^4	10^4
Thermal contact resistance of hot-side ($\text{W/m}^2\text{K}$)	6×10^4	6×10^4	6×10^4
Average Seebeck coefficient (mV/K) p, n	144, -185	168, -198	189, -210
Average electrical resistivity (mW cm) p, n	0.89, 1.24	1.13, 1.41	1.42, 1.65
Average thermal conductivity ($\text{W/m}^2\text{K}$) p, n	1.18, 1.3	1.09, 1.22	1.01, 1.15

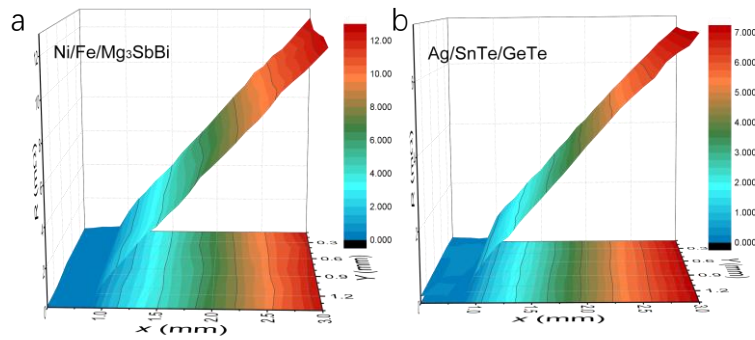


Fig. S12. Mapping of resistance across the Ni/Fe/ Mg_3SbBi (a) and Ag/SnTe/GeTe (b) interfaces.

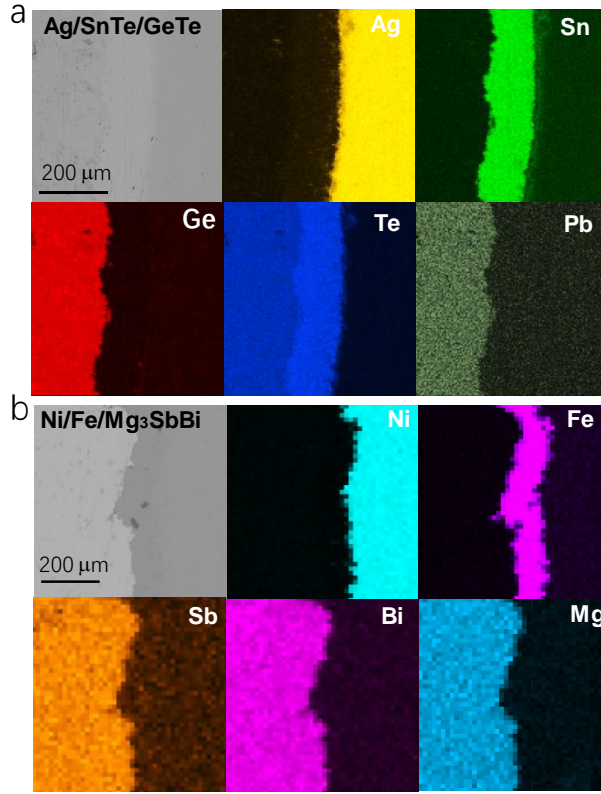


Fig. S13. SEM images and EDS mapping for hot-pressed Ag/SnTe/GeTe (a) and Ni/Fe/Mg₃SbBi contacts (b).

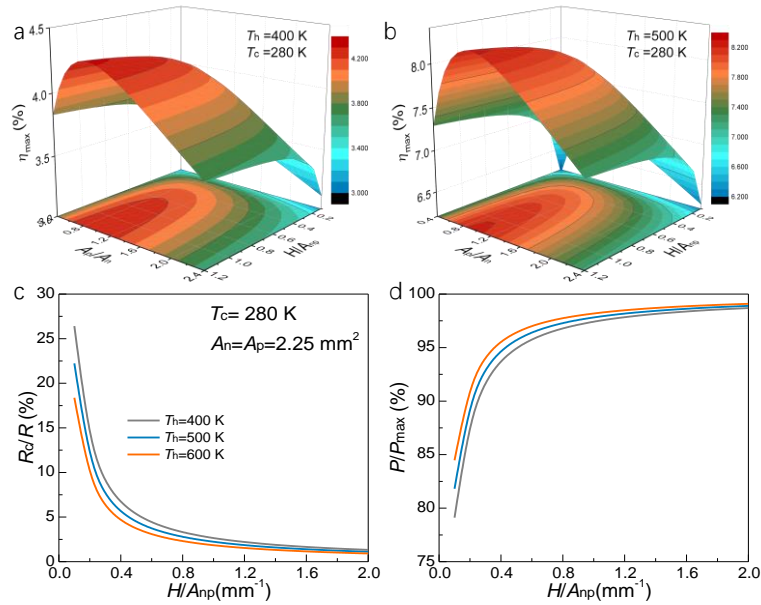


Fig. S14. Simulated maximum efficiency (η_{\max}) as a function of the cross-sectional area ratio (A_p/A_n) of p- to n-type leg's and the ratio of height to the total cross-sectional area of a pair of legs (H/A_{pn}) for the GeTe/Mg₃SbBi module (a, b). Interfacial contact resistance accounts for the total resistance (R_c/R) (c), the corresponding reduction in relative output power (P/P_{\max}) (d) as a function of H/A_{pn} .

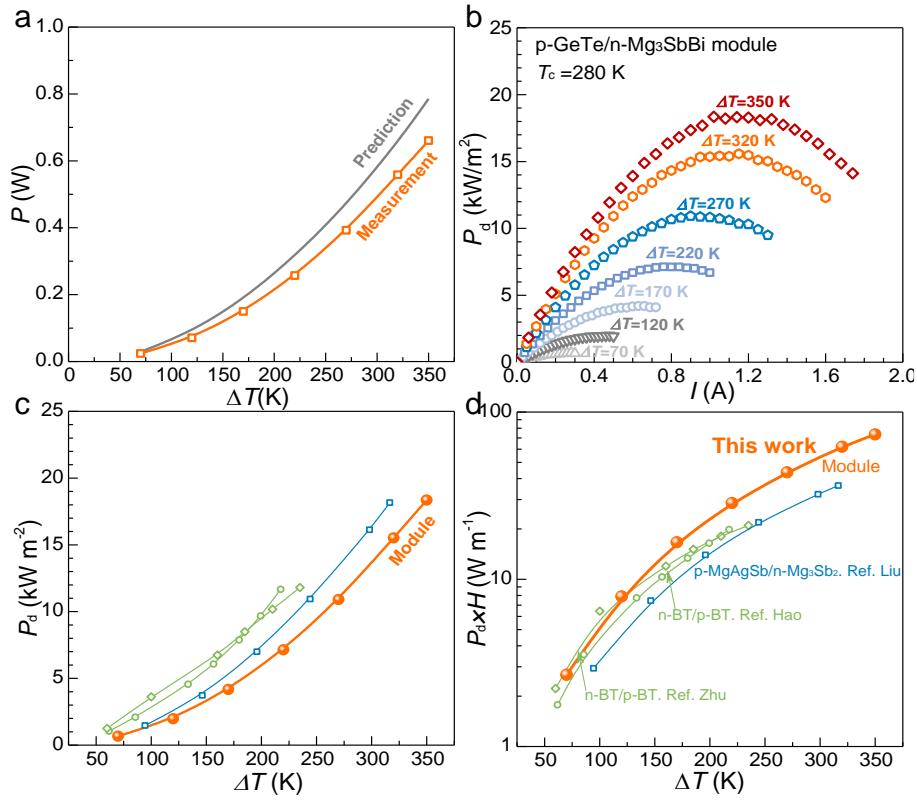


Fig. S15. Temperature gradient dependent the output power (P) compare with the prediction (a), the output power density (P_d) (c), the specific power density ($P_d \times H$) (d), and current dependent output power density (P_d) (b).

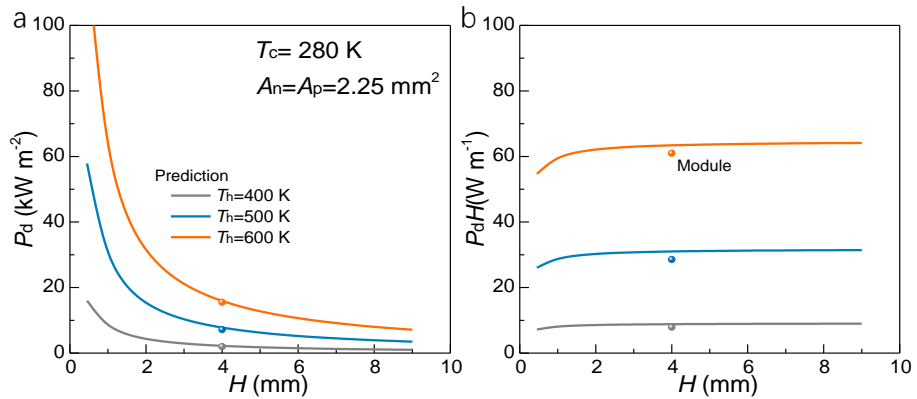


Fig. S16. The output power density (P_d) (a), and specific power density $P_d \times H$ (b) as a function of leg height of thermoelectric materials. The curves show the predictions according to the properties of thermoelectric materials and the contact resistance.

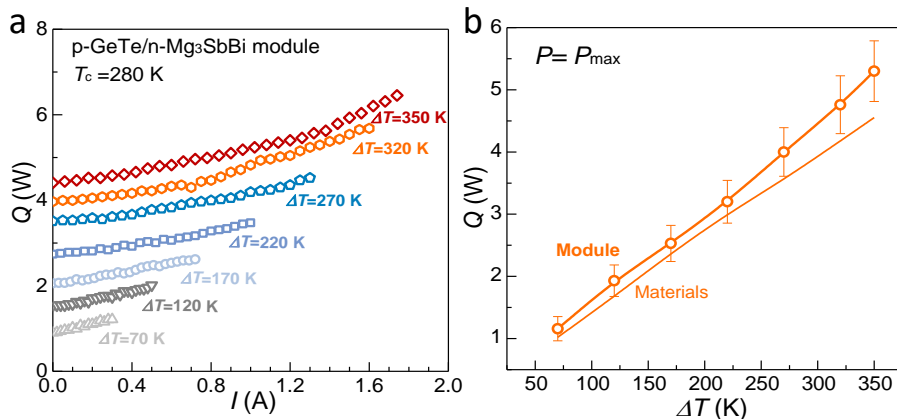


Fig. S17. Current (I) dependent measured heat flow (Q) (a), temperature gradient dependent measurement and prediction of the heat flow (Q) at $P = P_{max}$.

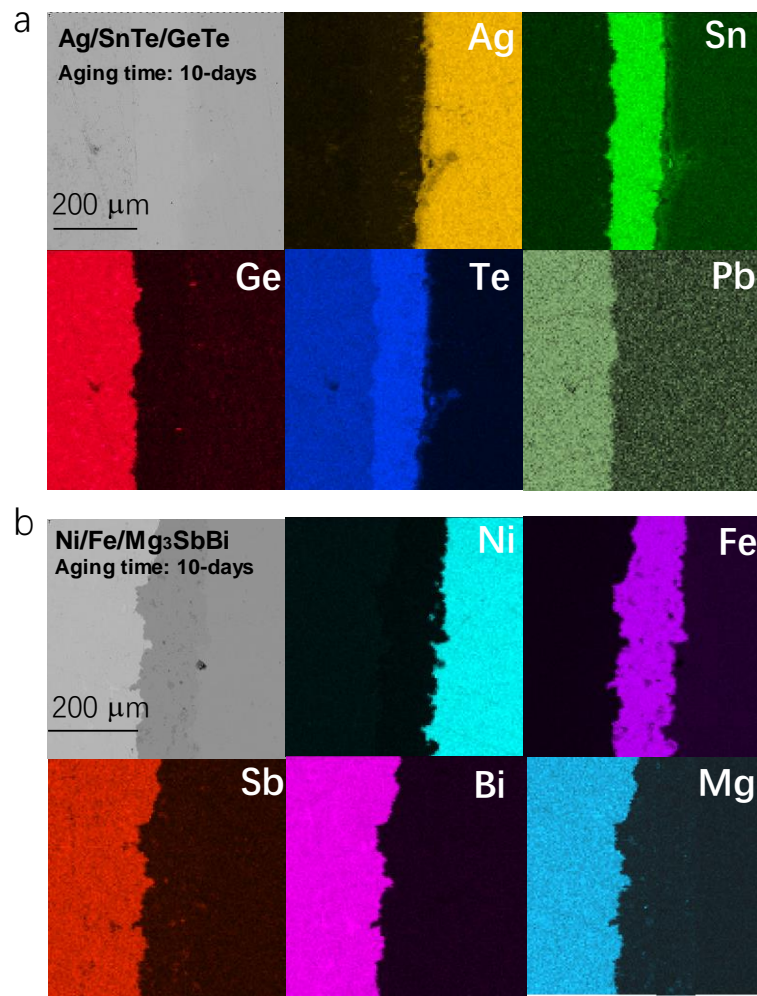


Fig. S18. SEM images and EDS mapping of the Ag/SnTe/GeTe (a) and Ni/Fe/Mg₃SbBi (b) contacts after 10-days aging at 600 K.

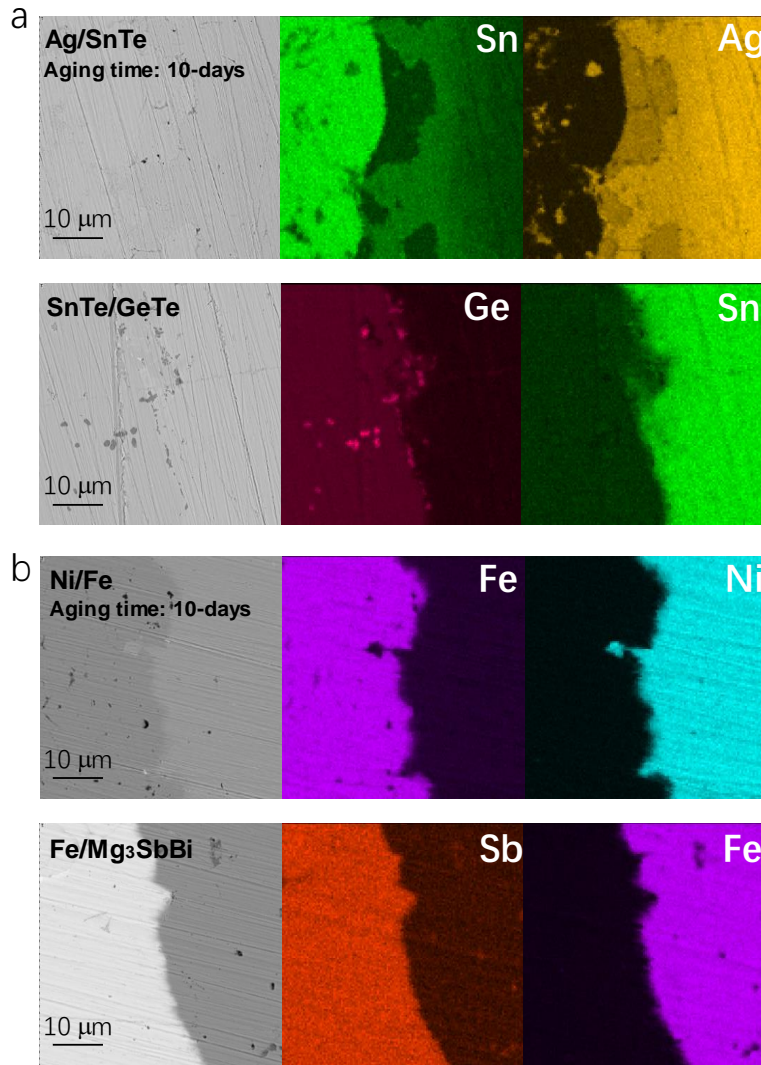


Fig. S19. SEM images and EDS mapping of the Ag/SnTe/GeTe (a) and Ni/Fe/Mg₃SbBi (b) contacts after 10-days aging at 600

K.

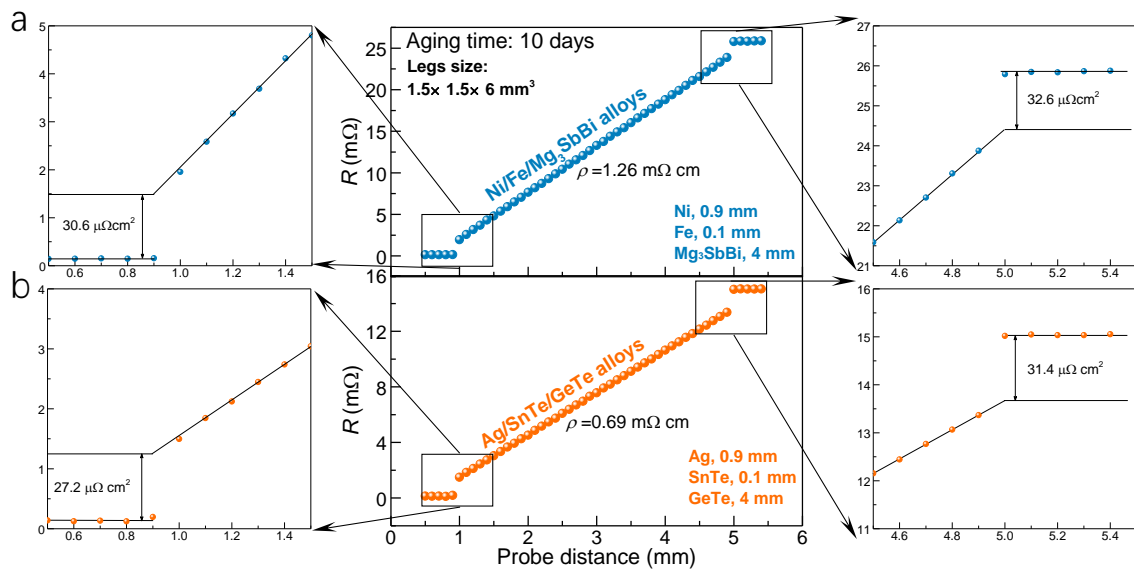


Fig. S20. Line scanning of resistance across the Ag/SnTe/GeTe (a) and Ni/Fe/Mg₃SbBi (b) interfaces after 10-days aging at 600 K for estimating the contact resistance and the resistivity of the thermoelectric materials.

References

1. W. Li, L. Zheng, B. Ge, S. Lin, X. Zhang, Z. Chen, Y. Chang and Y. Pei, *Adv Mater*, 2017, **29**.
2. Z. Bu, X. Zhang, B. Shan, J. Tang, H. Liu, Z. Chen, S. Lin, W. Li and Y. Pei, *Science Advances*, 2021, **7**, eabf2738.
3. Z. Liang, C. Xu, H. Shang, Q. Zhu, F. Ding, J. Mao and Z. Ren, *Materials Today Physics*, 2021, **19**, 100413.
4. D. Kraemer, J. Sui, K. McEnaney, H. Zhao, Q. Jie, Z. F. Ren and G. Chen, *Energ Environ Sci*, 2015, **8**, 1299-1308.
5. Q. Zhu and Z. Ren, *Energy*, 2020, **191**, 116599.
6. SAGROEN, Conventional Generating Devices (TEG), <http://e.hbsagreon.com/teg.html>, (accessed July, 2021).
7. E. Alleno, N. Lamquembe, R. Cardoso-Gil, M. Ikeda, F. Widder, O. Rouleau, C. Godart, Y. Grin and S. Paschen, *physica status solidi (a)*, 2014, **211**, 1293-1300.
8. J. Yu, Y. Xing, C. Hu, Z. Huang, Q. Qiu, C. Wang, K. Xia, Z. Wang, S. Bai, X. Zhao, L. Chen and T. Zhu, *Advanced Energy Materials*, 2020, **10**, 2000888.
9. P. Jood, M. Ohta, A. Yamamoto and M. G. Kanatzidis, *Joule*, 2018, **2**, 1339-1355.
10. F. Hao, P. Qiu, Y. Tang, S. Bai, T. Xing, H.-S. Chu, Q. Zhang, P. Lu, T. Zhang, D. Ren, J. Chen, X. Shi and L. Chen, *Energ Environ Sci*, 2016, **9**, 3120-3127.
11. H. Zhu, R. He, J. Mao, Q. Zhu, C. Li, J. Sun, W. Ren, Y. Wang, Z. Liu, Z. Tang, A. Sotnikov, Z. Wang, D. Broido, D. J. Singh, G. Chen, K. Nielsch and Z. Ren, *Nat Commun*, 2018, **9**, 2497.
12. T. Xing, Q. Song, P. Qiu, Q. Zhang, M. Gu, X. Xia, J. Liao, X. Shi and L. Chen, *Energ Environ Sci*, 2021, DOI: 10.1039/d0ee02791j.
13. P.-a. Zong, R. Hanus, M. Dylla, Y. Tang, J. Liao, Q. Zhang, G. J. Snyder and L. Chen, *Energ Environ Sci*, 2017, **10**, 183-191.
14. B. Poudel, Q. Hao, Y. Ma, Y. Lan, A. Minnich, B. Yu, X. Yan, D. Wang, A. Muto, D. Vashaee, X. Chen, J. Liu, M. S. Dresselhaus, G. Chen and Z. Ren, *Science*, 2008, **320**, 634-638.
15. L. Hu, F. Meng, Y. Zhou, J. Li, A. Benton, J. Li, F. Liu, C. Zhang, H. Xie and J. He, *Adv Funct Mater*, 2020, DOI: 10.1002/adfm.202005202, 2005202.
16. S. Lin, W. Li, S. Li, X. Zhang, Z. Chen, Y. Xu, Y. Chen and Y. Pei, *Joule*, 2017, **1**, 816-830.
17. K. Imasato, S. D. Kang and G. J. Snyder, *Energ Environ Sci*, 2019, **12**, 965-971.
18. W. Liu, H. S. Kim, S. Chen, Q. Jie, B. Lv, M. Yao, Z. Ren, C. P. Opeil, S. Wilson, C. W. Chu and Z. Ren, *Proc Natl Acad Sci U S A*, 2015, **112**, 3269-3274.
19. Y. Xiao, Y. Wu, P. Nan, H. Dong, Z. Chen, Z. Chen, H. Gu, B. Ge, W. Li and Y. Pei, *Chem*, 2020, **6**, 523-537.
20. B. Zhu, X. X. Liu, Q. Wang, Y. Qiu, Z. Shu, Z. T. Guo, Y. Tong, J. Cui, M. Gu and J. Q. He, *Energ Environ Sci*, 2020, **13**, 2106-2114.